

LA-UR-15-27239 (Accepted Manuscript)

On the formation and origin of substorm growth phase/onset auroral arcs inferred from conjugate space-ground observations

Motoba, T.
Ohtani, S.
Anderson, B. J.
Korth, H.
Mitchell, D.
Lanzerotti, L. J.
Shiokawa, K.
Connors, M.
Kletzing, C. A.
Reeves, Geoffrey D.

Provided by the author(s) and the Los Alamos National Laboratory (2016-06-22).

To be published in: Journal of Geophysical Research: Space Physics

DOI to publisher's version: 10.1002/2015JA021676

Permalink to record: <http://permalink.lanl.gov/object/view?what=info:lanl-repo/lareport/LA-UR-15-27239>

Disclaimer:

Approved for public release. Los Alamos National Laboratory, an affirmative action/equal opportunity employer, is operated by the Los Alamos National Security, LLC for the National Nuclear Security Administration of the U.S. Department of Energy under contract DE-AC52-06NA25396. Los Alamos National Laboratory strongly supports academic freedom and a researcher's right to publish; as an institution, however, the Laboratory does not endorse the viewpoint of a publication or guarantee its technical correctness.

**On the formation and origin of substorm growth
phase/onset auroral arcs inferred from conjugate
space-ground observations**

T. Motoba^{1, 2}, S. Ohtani¹, B. J. Anderson¹, H. Korth¹, D. Mitchell¹, L. J.
Lanzerotti³, K. Shiokawa⁴, M. Connors⁵, C. A. Kletzing⁶, and G. D. Reeves⁷

Update: September 6, 15

Correspondence to:

T. Motoba, Solar–Terrestrial Environment Laboratory, Nagoya University,
Furo-cho, Chikusa-ku, Nagoya, 464-8601, Japan (tetsuo.motoba@gmail.com)

¹ The Johns Hopkins University Applied Physics Laboratory
Laurel, MD, USA

² Now at Solar–Terrestrial Environment Laboratory, Nagoya University,
Nagoya, Japan

³ New Jersey Institute of Technology,
Newark, New Jersey, USA

⁴ Solar–Terrestrial Environment Laboratory, Nagoya University,
Nagoya, Japan

⁵ Athabasca University, Alberta AB, Canada

⁶ Department of Physics and Astronomy, University of Iowa,
Iowa City, Iowa, USA

⁷ Space and Atmospheric Sciences Group, Los Alamos National Laboratory,
Los Alamos, New Mexico, USA

Abstract. Magnetotail processes and structures related to substorm growth phase/onset auroral arcs remain poorly understood mostly due to the lack of adequate observations. In this study we make a comparison between ground-based optical measurements of the premidnight growth phase/onset arcs at subauroral latitudes and magnetically conjugate measurements made by the Active Magnetosphere and Planetary Electrodynamics Response Experiment (AMPERE) at ~ 780 km in altitude and by the Van Allen Probe-B (RBSP-B) spacecraft crossing L values of ~ 5.0 – 5.6 in the premidnight inner tail region. The conjugate observations offer a unique opportunity to examine the detailed features of the arc location relative to large-scale Birkeland currents and of the magnetospheric counterpart. Our main findings include (1) At the early stage of the growth phase the quiet auroral arc emerged $\sim 4.3^\circ$ equatorward of the boundary between the downward Region-2 (R2) and upward Region-1 (R1) currents; (2) Shortly before the auroral breakup (poleward auroral expansion) the latitudinal separation between the arc and the R1/R2 demarcation narrowed to $\sim 1.0^\circ$; (3) RBSP-B observed a magnetic field signature of a local upward field-aligned current (FAC) connecting the arc with the near-Earth tail when the spacecraft footprint was very close to the arc; and (4) The upward FAC signature was located on the tailward side of a local plasma pressure increase confined near $L \sim 5.2$ – 5.4 . These findings strongly suggest that the premidnight arc is connected to highly localized pressure gradients embedded in the near-tail R2 source region via the local upward FAC.

30 **Key words:** growth phase/onset arc, FACs, M-I coupling,

31 **Key points:**

- 32 • Conjugate space-ground observations of growth phase/onset arcs are examined
- 33 • AMPERE allows us to compare the arc location with dynamic large-scale FACs
- 34 • RBSP-B provides in situ measurements from the magnetospheric source region

1. Introduction

During the growth phase of geomagnetic substorms, quiet, latitudinally narrow, east-west elongated auroral arcs (often called "growth phase arc" or "preexisting arc") spontaneously emerge in the midnight sector and then gradually move equatorward. Around the auroral substorm onset, the most equatorward arc usually becomes active with sudden brightening and azimuthal structuring, eventually followed by auroral breakup and auroral poleward expansion. Whereas such morphological evolution of the growth phase arc and subsequent active arc (onset arc) is widely accepted through numerous observations of ground-based auroral images by early studies [e.g., *Akasofu*, 1964], the origin of the growth phase arc remains poorly understood in terms of source location and formation mechanism.

There are two key features of growth phase/onset arcs reported from prior studies [e.g., *Mende et al.*, 2003; *Dubyagin et al.*, 2003; *Yago et al.*, 2005, 2007; *Lessard et al.*, 2007; *Sergeev et al.*, 2012; *Jiang et al.*, 2012]. First, the arcs are attributed to inverted-V electron precipitation with a characteristic energy from a few hundred eV to a few keV electrons. This suggests that some process in the auroral acceleration region ($\sim 1\text{--}3 R_E$) is required to account for the arc formation. Second, the electron precipitation responsible for the arcs is located just poleward of the peak in the concurrent proton auroral precipitation, which is often interpreted as the proton isotropic boundary. This result suggests that the electron arcs are magnetically mapped to the transition region ($\sim 8\text{--}10 R_E$ in the magnetotail direction) in which the magnetic field topology changes from dipole-like to more tail-like.

As an alternative, a few recent case studies [*Shiokawa et al.*, 2005; *Marghitu et al.*, 2009; *Jiang et al.*, 2012; *Nishimura et al.*, 2012] have attempted to deduce the source region of

the arcs by comparing the arc location with large-scale Birkeland current regions, often referred to as Region-1 (R1) and Region-2 (R2) field-aligned currents (FACs) of which the behaviors are controlled by different source regions in the magnetosphere (or ionosphere) [e.g., *Iijima and Potemra*, 1978]. *Shiokawa et al.* [2005], *Marghitu et al.* [2009], and *Jiang et al.* [2012] pointed out that the premidnight arcs are located near the R1/R2 FAC boundary or within the upward R1 FAC. A similar conclusion was reached by *Ohtani et al.* [2010], from a statistical analysis of magnetic field and particle precipitation data sets from the DMSP spacecraft. Specifically, the statistics revealed a tendency for the occurrence of the most equatorward monoenergetic electron acceleration events (called "b3a boundary": see *Newell et al.* [1996] for more details of the definition) in the dusk-to-midnight sector to the peak in the upward R1 current.

In contrast, *Nishimura et al.* [2012], who examined four conjunction events in which the CHAMP satellite passed over an onset arc, reported that the arc-related FACs are formed within the downward R2 FAC. They also found that the arc location relative to the R1/R2 FAC distribution depends on the distance from the onset meridian: the arc location is within the downward R2 FAC region near the onset meridian, whereas it is close to the R1/R2 boundary on the east/west side of the onset meridian. Because of the lack of reliable samples to test where and how the arc develops with respect to the R1 and R2 current distribution, however, the debate about the origin is ongoing. In addition, the time-dependent behavior is observationally unclear because of a one-off arc crossing measurement with a single low-altitude spacecraft at certain times of the growth phase.

Some of the onset arc features in the ionosphere shown by *Nishimura et al.* [2012] were

reproduced by a recent high-resolution simulation with the Rice Convection Model-Equilibrium (RCM-E) by *Yang et al.* [2013]. The RCM-E simulation also predicted that in the premidnight sector the arc-related upward FAC is connected to localized pressure gradients around the inner edge of the plasma sheet, $\sim 8 R_E$ tailward. Missing until now have been simultaneous in situ measurements in the exact conjugate region of the magnetotail to test such modeling results.

In this study, we present a very fortuitous space-ground conjunction event of the premidnight growth phase/onset arcs that occurred on 1 May 2013. The arc evolution by subauroral-latitude all-sky imagers (ASI) of the Time History of Events and Macroscale Interactions during Substorms Ground Based Observatories (THEMIS GBOs) is compared with space-based measurements from both the magnetosphere and ionosphere regions that are magnetically conjugate to the arc. The Active Magnetosphere and Planetary Electrodynamics Response Experiment (AMPERE) provides a time-dependent map of the large-scale FAC distribution in the ionosphere at ~ 780 km altitude during the arc evolution. The Van Allen Probe-B spacecraft provides in situ field and plasma measurements from the magnetospheric source region at $L \sim 5.0$ – 5.6 . Through the ground-based ASI observations of visible aurora together with these simultaneous conjugate space-based observations, we discuss the magnetosphere-ionosphere (M-I) coupling processes involved in the generation of the growth phase/onset arcs.

Section 2 of this paper describes the data sets used in this study. Section 3 gives observational results of the 1 May 2013 substorm event based on analysis of the ground-based and space-based observations. Section 4 discusses the implications of the

observations and summarizes our findings.

2. Data Sets

The primary sources of data used in this study are the THEMIS GBOs [Mende *et al.*, 2008; Russell *et al.*, 2008], AMPERE [Anderson *et al.*, 2014; and references therein], and probe B of the Van Allen Probes mission (also known as the Radiation Belt Storm Probes: RBSP for the abbreviated name) [Mauk *et al.*, 2013].

Each of the THEMIS GBOs has a set of white light all-sky imager (ASI; 3-s sampling) and fluxgate magnetometer (0.5-s sampling). In this study, we used the ASI data from three central Canadian stations of the THEMIS GBOs, Athabasca (ATHA, 54.7°N, 246.7°E, magnetic latitude (MLAT) = 62.2°N, magnetic local time (MLT) = UT–08:18), Fort Smith (FSMI, 60.0°N, 248.1°E, MLAT = 67.6°N, MLT = UT–08:19), and The Pas (TPAS, 54.0°N, 259.1°E, MLAT = 63.4°N, MLT = UT–07:10). MLAT and MLT are represented in Altitude Adjusted Corrected Geomagnetic (AACGM) coordinates [Baker and Wing, 1989]. The three ASIs are partially spatially overlapping, allowing the capture of visible auroral evolution over a wider area than would a single field-of-view (FOV) ASI.

AMPERE provides global maps of large-scale Birkeland currents or field-aligned currents (FACs) in both hemispheres at a cadence of 10 min derived through a spherical harmonic fit to the magnetic field perturbation ($\delta\mathbf{B}$) data obtained from the Iridium Communications satellite constellation. The constellation consists of more than 66 polar-orbiting satellites in circular polar orbits with 780 km altitude and 86° inclination, configured in six orbit planes

equally spaced in longitude. In addition to the global maps of FAC patterns, the AMPERE raw $\delta\mathbf{B}$ data (sampling resolution of 19.44 s, corresponding to a latitudinal resolution of about 1.3°) were also used to characterize the detailed latitudinal profile of large-scale FACs along the premidnight meridian at a time when an Iridium vehicle passed across the growth phase/onset arc presented herein.

In situ particle and magnetic and electric field data were obtained from the following instruments onboard the RBSP-B spacecraft: Radiation Belt Storm Probes Ion Composition Experiment (RBSPICE) [Mitchell *et al.*, 2013], Electric and Magnetic Field Instrument Suite and Integrated Science (EMFISIS) magnetometer instrument [Kletzing *et al.*, 2013], and Helium Oxygen Proton Electron (HOPE) instrument [Funsten *et al.*, 2013]. RBSPICE proton flux data for lower (10–50 keV) and higher (above 60 keV up to a few MeV) energies are collected by the ToF by Pulse Height (ToF×PH) proton rates product and ToF by Energy (ToF×E) proton rates product, respectively (see Mitchell *et al.* [2013] for more details). A low pass filter was used to remove an 11-s spin tone signal from the EMFISIS magnetic field (\mathbf{B}) vector data. HOPE can provide "partial" proton pressure derived from the proton flux measurements from 30 eV up to 40 keV. It should be noted here that, in this study the HOPE proton pressure was multiplied by a factor of 3 based on a calibration analysis result made by the HOPE team [J. Reeves, *private communications*, 2015].

Figures 1a and 1b show the location of the RBSP-B spacecraft for 05:30–07:00 UT on 1 May 2013 in the x - y and x - z planes in solar magnetic (SM) coordinates, respectively, with solid circle tick marks indicating the satellite's position at 30-min intervals. Also indicated in Figure 1b for reference are magnetic field lines derived from the Tsyganenko 1996 (T96)

model [Tsyganenko and Stern, 1996]. During this interval the RBSP-B spacecraft moved tailward and slightly northward toward apogee in the premidnight sector inner magnetosphere, and in the off-equatorial plane $\sim 10^\circ$ away from the equator.

Figure 1c presents the three THEMIS ASI FOVs of ATHA, FSMI and TPAS, together with the magnetic footprint of the RBSP-B spacecraft during the interval of 05:30–07:00 UT and with the premidnight AMPERE tracks at the early (i), middle (ii), late (iii) stages of the substorm growth phase (further details in section 3). The RBSP-B footprint, computed at an altitude of 110 km using the T96 model, is displayed with locations at the same intervals as Figures 1a and 1b. The footprint calculation was made by taking the following fixed input parameters ($Dst = -24$ nT, solar wind dynamic pressure = 2.1 nPa, interplanetary magnetic field (IMF) $B_y = -3.1$ nT, and IMF $B_z = -9.9$ nT). Each parameter was obtained by averaging the values of the 5-min OMNI data for 06:00–06:30 UT, covering the entire development of growth phase/onset arcs. For this event the T96 model was used for the footprint estimate because the T96 model performance at RBSP-B was better than the newer version (TS04 model, [Tsyganenko and Sitnov, 2005]). The performance comparison will be presented in section 3.4.

In addition to the THEMIS ASIs, the other ground-based sources of data were acquired from a high sensitivity all-sky imager at ATHA and from SuperMAG in order to complement the space-based data sources. The all-sky imager has been operated as part of the Optical Mesosphere Thermosphere Imagers (OMTI) project of the Solar-Terrestrial Environment Laboratory, Nagoya University [Shiokawa *et al.*, 2009]. The OMTI ASI uses a thinned and back-illuminated cooled charge coupled device (CCD) with 512×512 pixels

and has seven interference filters including wavelengths of 557.7 nm (O, filter bandwidth: 1.76 nm), 630.0 nm (O, 1.64 nm), 720–910 nm (infrared OH-band), 486.1 nm (H β , 1.32 nm), 572.5 nm (background), 844.6 nm (O, 1.30 nm), and 589.3 nm (Na, 1.56 nm). In this study we used the OMTI 557.7 nm (exposure time of 5 s) and H β (exposure time of 25 s) auroral images with a time resolution of 2 min and 2×2 binning of the CCD pixels (256×256 in total) to identify auroral features due to electron and proton precipitations.

SuperMAG, which is a global magnetometer network initiative, provides 1-min ground-based magnetometer data at more than 300 stations obtained throughout a worldwide collaboration of organizations and national agencies [Gjerloev, 2009]. The SuperMAG data have an identical format organized in the same coordinate system (*NEZ* coordinates) and processed with a common baseline removal technique [Gjerloev, 2012] in which the baselines (such as daily variations and yearly trend) have been subtracted from the original data. Here the *N*-component is directed toward local magnetic north, *E*-component local magnetic east, and *Z*-component vertically down. In this study we used the individual SuperMAG magnetometer data at 11 stations: 3 out of 11 are colocated at the THEMIS ASI stations (ATHA, TPAS, and FSMI) used here, while the other 8 stations are located in the auroral–subauroral zone near the ATHA–FSMI geomagnetic meridian. In addition, the SuperMAG auroral electrojet indices at 1 min cadence [Newell and Gjerloev, 2011a, 2011b], referred to as "SMU" and "SML" (corresponding to traditional AU and AL, respectively), were also used. The SMU/SML indices are deduced from 100 or more sites of the SuperMAG data base in the MLAT range of 40–80° which include the standard 12 auroral-zone stations used to derive the AU/AL indices. Such dense longitudinal and

latitudinal coverage of the magnetometer data is particularly important for monitoring the development of auroral electrojets at a time when the auroral activity is spatially localized or when the auroral oval expands towards lower latitudes.

3. Observations

3.1. Solar Wind And Geomagnetic Activity

Figure 2 shows the strength ($|B|$; Figure 2a), and B_y and B_z components (Figure 2b) of the IMF in geocentric solar magnetospheric (GSM) coordinates obtained from the 1-min resolution OMNI database, SuperMAG auroral electrojet indices, SMU and SML (Figure 2c), and SYM H index (Figure 2d) for 00:00–12:00 UT on 1 May 2013. The gray-shaded area of 05:30–07:00 UT is the interval of interest. Throughout this interval the solar wind speed and dynamic pressure remained almost at a constant value of $\sim 400 \text{ km s}^{-1}$ and $\sim 2.1 \text{ nPa}$, respectively (not shown here). As seen in Figure 2b, the IMF B_z component was southward (around -5 nT) for most of ~ 5 hours before the interval of interest, except for the very short times of its northward excursions. During the interval of interest the IMF B_z underwent quasi-steady southward conditions with larger negative values (around -10 nT) than for the prior interval. Such strong southward IMF B_z conditions enhance magnetospheric and ionospheric convections responsible for the strengthening of eastward (westward) electrojet in the evening (morning) auroral zone [Weimer, 1994; Gjerloev *et al.*, 2004], that is, the growth phase of a geomagnetic substorm. Indeed, corresponding to the eastward (westward) electrojet intensification, the SMU (SML) index gradually increased

(decreased) from ~ 250 nT to ~ 400 nT (from ~ -160 nT to ~ -340 nT) after $\sim 05:45$ UT. It should also be noted that the substorm growth phase occurred in the course of the main phase of a moderate geomagnetic storm, as is evident in Figure 2d.

The substorm expansion phase started around 06:25 UT, which was identified by SMLd (blue curve in Figure 2c) that detected a small negative bay from ~ -100 nT to ~ -270 nT. SMLd is the "darkness" SML index derived only from data at stations located in the dark hemisphere (solar zenith angle $> 104^\circ$ at an altitude of 200 km) in the MLAT range of $40\text{--}80^\circ$. An advantage of SMLd is to enable adequate capture of an explosive development of nightside westward electrojet at the onset of the substorm expansion phase, because SMLd is less affected by the growth phase-related westward electrojet in the morning sector. Indeed, the onset of the substorm expansion phase deduced from SMLd is in good agreement with the onset of visible auroral breakup that is shown in section 3.2.

3.2. THEMIS ASI Observations: Growth Phase/Onset Arcs

The spatiotemporal evolution of visible aurora for the 1 May 2013 substorm event was observed with three neighboring THEMIS ASIs at FSMI, ATHA, and TPAS in the premidnight auroral-subauroral region (Figure 1c). We note that some of the stations had slightly and partially cloudy skies, but there was little effect on the optical analysis presented herein. Figure 3 presents an overview of the premidnight auroral evolution from the ASIs and relevant electrojets deduced from the ground magnetometers. The ASI snapshots (Figures 3a-3d) on the left depict 2-dimensional (2D) signatures of the auroral

substorm, including poleward boundary intensification (PBI)/streamer, growth phase arc, and auroral breakup. For a reference the RBSP-B footprint (red circle) at each time is also superimposed onto the image. Shown on the right are keograms (Figure 3e-3g) and magnetograms (Figures 3h-3i) obtained from the three stations for the interval of 05:30–07:00 UT, in order to illustrate a time sequence of the auroral substorm. The vertical dashed line marks the onset time (06:24:36 UT) of the auroral breakup (poleward auroral expansion) determined from the ASI at TPAS. The color-coded horizontal dashed line in each of Figures 3e-3g is drawn at MLAT of each station: FSMI (yellow), ATHA (red), and TPAS (blue).

The auroral keogram from FSMI (Figure 3e), which covers the poleward portion of the auroral oval, displays successive PBIs/streamers during the growth phase, at least ~20 min prior to the auroral breakup at 06:24:36 UT. The streamers propagated equatorward at a speed of 0.5–1.5 km s⁻¹, slightly slower than the average speed (2.0 km s⁻¹) reported by *Nishimura et al.* [2010] for such streamers. Whereas most of the equatorward propagating streamers faded around 66° MLAT, the brighter streamers that started a few minutes before the onset penetrated further equatorward up to ~63–64° MLAT.

On the other hand, the keograms from both ATHA (Figure 3f) and TPAS (Figure 3g), which cover the equatorward portion of the auroral oval, captured simultaneously the development of a quiet, east-west elongated growth phase arc which was located in the MLAT range of ~62–63° and in the MLT range of ~21:30–23:30 MLT. The 2D signatures can also be seen in Figures 3a-3c. After ~06:00 UT the growth phase arc gradually moved equatorward from ~63° MLAT and around 06:20 UT the arc location lowered to ~62° MLAT. The arc location

was very close to the zenith of ATHA, while it was $\sim 1.0^\circ$ or more equatorward of the zenith of TPAS (It should be noted here that the latitudinal arc width at TPAS apparently becomes thicker than that at ATHA because the distortion of the all-sky image caused by the fish-eye lens increases toward the edge of the FOV). After that, the arc became more active with a sudden brightening and spatial structuring (or beading) [e.g., *Donovan et al.*, 2006; *Motoba et al.*, 2012]. The active arc just before the auroral breakup is referred to as "onset arc". For this event, it is interesting that the arc beading appeared to begin before the brighter streamers reached near the arc region, although the detailed discussion is beyond the main scope of this work.

Figure 3h (3i) shows the *N*-component (*Z*-component) of the magnetic field at FSMI (yellow curve), ATHA (red curve), and TPAS (blue curve) to monitor the behavior of auroral electrojets associated with the poleward boundary auroral activation and the growth phase/onset arc evolution. During the growth phase, the *N*-component at FSMI had almost constant positive values with amplitude of ~ 100 nT. Such a positive *N*-component at FSMI may arise from the presence of the eastward electrojet flowing near FSMI. The location of the eastward electrojet relative to the station can be inferred from the *Z*-component variation. During the same interval the *Z*-component at FSMI was negative, suggesting that the eastward electrojet was located equatorward of FSMI. Just before the auroral breakup onset, the *N*-component at FSMI turned from positive to zero or negative, while the *Z*-component crossed zero and then became positive. This suggests that westward electrojet strengthened around FSMI, instead of the eastward electrojet. The temporal evolution of the electrojets monitored at FSMI coincided well with that of auroral activity at or near the

poleward boundary of the auroral oval, shifting from $\sim 69^\circ$ MLAT to near the zenith of FSMI as the growth phase progressed (Figure 3e).

We next consider the behavior of auroral electrojets associated with the growth phase arc evolution, based on the magnetograms at ATHA and TPAS. During the growth phase, the N -component at ATHA gradually increased by ~ 50 nT, while at TPAS the N -component decreased. The N -component change at ATHA (TPAS) may be attributed to the enhancement of the eastward (westward) electrojet flowing on the equatorward (poleward) side of the arc. At the same time the Z -component at ATHA began to decrease as the arc became closer to ATHA. This suggests that at the late stage of the growth phase the eastward electrojet was located just equatorward of the zenith of ATHA. On the other hand, the Z -component at TPAS increased during the growth phase, suggesting that the westward electrojet was located equatorward of TPAS.

When the onset arc developed, a small decrease in the N -component began only at TPAS closer to the breakup region. After the auroral breakup onset the N -component at TPAS developed into a negative magnetic bay with magnitude of ~ 250 nT. In this study we focus on the time interval from the beginning of the growth phase up to just before the auroral breakup.

Figure 4 displays a time sequence of 2D auroral images at ATHA (left) and TPAS (right) for 06:15–06:25 UT, focusing attention on the auroral arc evolution from the growth phase arc to the onset of the auroral expansion. Each of the ATHA (TPAS) images that capture the arcs is cropped from the roughly central (bottom) one-fourth portion of the original all-sky image. Superimposed on each image are the equi-contours of 62.0° , 62.5° , and 63.0° MLAT,

projected at an altitude of 110 km. The RBSP-B footprint (determined from T96) at each time is marked by the red circles in the ATHA image.

As can be seen in Figure 4, the east-west aligned arc observed with ATHA and TPAS was within the same latitudinal range of 62.0° and 62.5° MLAT. Around 06:19 UT, although the arc luminosity remained almost unchanged, both ASIs detected the first visible indication of a beading/ray structure which spontaneously emerged along the preexisting arc and started to move in the eastward direction along the arc. About 1 min later (~ 0620 UT), an initial brightening appeared in the structuring arc. This time may be regarded as the "onset epoch", according to the classical definition by *Akasofu* [1964]. At 06:25 UT, a part of the active onset arc around $23:00$ MLT expanded poleward with much stronger auroral brightening (see the TPAS image). The observed auroral arc evolution is generally similar to the morphology of typical auroral substorms obtained from previous ground-based observations [*Akasofu*, 1964], except for the onset location occurring at lower latitude than the statistical onset location ($\sim 66.4^\circ$) reported by *Frey et al.* [2004]. Taking into account that the IMF B_z had quasi-stable negative values around -10 nT during this event (Figure 2a), it seems quite reasonable that the onset location was lower than the typical subauroral latitudes [cf. *Liou et al.*, 2001].

3.3. AMPERE Observations: Large-Scale FACs

As can be seen in Figure 1c, during the growth phase three successive orbital tracks of AMPERE crossed over the FSMI–ATHA FOVs in the premidnight sector. In the top

(bottom) panel of Figure 5 we make a 2D comparison of the AMPERE-derived FAC patterns for 06:12–06:22 UT (06:20–06:30 UT) and auroral images at 06:16 UT (06:24 UT) (see Movie S1 for the entire time sequence at 2-min intervals). The red and blue contours represent upward and downward FACs, respectively. Superimposed on the 2D snapshot at 06:16 UT (06:24 UT) for a reference are the raw $\delta\mathbf{B}$ (yellow) vectors obtained along the premidnight AMPERE orbital track for 06:14–06:18 UT (06:22–06:26 UT).

Typically, the large-scale FACs in the premidnight sector consist of a two-sheet structure, where the upward FAC on the poleward side and the downward FAC on the equatorward side are called Region-1 (R1) and Region-2 (R2), respectively. The 2D comparison at 06:16 UT indicates that, whereas brighter discrete auroral forms at the poleward boundary ($\sim 67\text{--}70^\circ$ MLAT) at least in part overlapped with the upward R1 FAC region, the faint growth phase arc at $\sim 62\text{--}63^\circ$ MLAT was located near the center of the downward R2 FAC. On the other hand, the 2D comparison at 06:24 UT, immediately before the auroral breakup, represents that the most equatorward brightening arc was closer to the R1/R2 demarcation.

Figure 6 presents detailed comparisons of the arc location with the latitudinal profiles of FACs at about 10-min intervals: the (i) early, (ii) middle, (iii) late stages of the growth phase according to the three successive passes of AMPERE. Shown in the panels from the top are (Figure 6a) the northward and eastward components of the AMPERE raw $\delta\mathbf{B}$ along the premidnight orbital track (the time stamps of the orbital track at each stage are marked in Figure 6a), (Figure 6b) the latitudinal profile of the auroral luminosity along the orbital track that is resampled at 3-s intervals with a linear interpolation, (Figure 6c) MLAT-MLT projection of the ATHA and FSMI auroral images at a time when the vehicle footprint was

closest to the arc, and (Figure 6d) latitudinal profiles of the magnetic N - and Z -component deviations derived from the 10 ground stations near the ATHA–FSMI meridian. Six out of the 10 stations (T35: Snap Lake, MEA: Meanook, C06: Ministik Lake, RED: Red Deer, T03: Vulcan, and LET: Lethbridge) are located within the MLT sector of ± 10 min from the meridian, whereas the other two stations, T42 (La Ronge) and YKC (Yellowknife), are separated by $\sim +45$ min and ~ -20 min in the MLT direction, respectively. Each latitudinal profile of the magnetic N - and Z -component deviations was estimated by averaging over a 5-min window: (i) 06:03 UT ± 2 min, (ii) 06:13 UT ± 2 min, and (iii) 06:22 UT ± 2 min. A spline fit was made for both the N and Z components. Both magnetic N - and Z -component profiles are used to deduce the central latitude of the eastward auroral electrojet [e.g., *Kisabeth and Rostoker, 1977*] that is manifested most likely between the R1 and R2 FACs in the premidnight sector during the growth phase. With the AMPERE $\delta\mathbf{B}$ data used in Figure 6a, it is not possible to identify fine-scale FAC signatures less than a latitudinal resolution of $\sim 1.3^\circ$ because of its sampling rate (19.44 s). Therefore, we use the AMPERE $\delta\mathbf{B}$ data only to describe large-scale FAC patterns, which correspond to major slopes of the eastward component of $\delta\mathbf{B}$. Here we assume that the large-scale FAC patterns remain unchanged during each pass (about 5 min).

At the early stage (i) of the growth phase, the faint arc was at $\sim 63.0^\circ$ MLAT (panels b and c), being $\sim 4.3^\circ$ equatorward of the AMPERE $\delta\mathbf{B}$ -deduced R1/R2 boundary at $\sim 67.3^\circ$ MLAT (panel a). This result indicates that the initial development of the growth phase arc began deep inside the downward R2 FAC region. The R1/R2 boundary also coincided with the central latitude of the eastward electrojet, which was deduced from a positive peak in the

N-component and a bipolar signature in the *Z*-component (panel d).

At the middle stage (*ii*) the arc location lowered to 62.3° MLAT (panels b and c), i.e., it shifted equatorward by $\sim 0.7^\circ$. The R1/R2 boundary (panel a) and eastward electrojet (panel d) also shifted equatorward by $\sim 2.5^\circ$ with respect to those at the early stage (*i*). It is interesting to note that the equatorward shift of the arc was much smaller (about one-third) than that of the R1/R2 boundary/eastward electrojet. At this stage, the arc location was closer to the R1/R2 boundary, but it still remained inside the downward R2 FAC region.

At the late stage (*iii*), the arc stayed almost at the same latitude (62.3° MLAT) as at the middle stage (panels b and c), although the arc luminosity was significantly enhanced. On the other hand, the latitudes of the R1/R2 boundary (panel a) and eastward electrojet (panel d) were positioned at $\sim 63.2^\circ$ MLAT. As a result, the latitudinal separation ($\sim 1.0^\circ$) between the arc location and R1/R2 boundary apparently became narrower than that at the middle stage. We note here that a decreasing slope in the eastward component of $\delta\mathbf{B}$ was much steeper in the R2 region than in the R1 region. The AMPERE-derived FAC patterns in Figure 5 suggest that the steeper $\delta\mathbf{B}$ slope was due to the strengthening of the R2 FAC intensity.

The simultaneous observations with AMPERE throughout the growth phase indicate that the location of the premidnight growth phase arc relative to the R1/R2 boundary changes within the downward R2 FAC region as the arc develops. This is the first time that such conditions have been reported. This suggests that the magnetospheric counterpart of the arc maps to the R2 FAC source region.

3.4. Van Allen Probe-B Observations: Magnetospheric Counterpart

At certain times of the growth phase the Van Allen Probe-B (RBSP-B) spacecraft was magnetically conjugate to the zenith of ATHA (see Figure 1). Therefore, the RBSP-B spacecraft observations provide a good opportunity to examine the detailed features of the magnetospheric counterpart of the arc.

Figure 7 presents the magnetic field measurements obtained from the RBSP-B EMFISIS instrument for the interval of 05:30–07:00 UT. Plotted from the top are the magnetic field strength ($|B|$, Figure 7a), the B_x (Figure 7b), B_y (Figure 7c), and B_z (Figure 7d) components in the GSM coordinate system, and the B_{x_FA} (Figure 7e) and B_{y_FA} (Figure 7f) components in the field-aligned (FA) coordinate system. (The large, very distinct ULF wave event at ~05:50 UT was discussed in *Motoba et al.* [2015].) In the FA coordinate system, the x component is in the radial direction (positive outward), while the y component is in the azimuthal direction (positive eastward). Both components are also orthogonal to the average direction parallel to the ambient local magnetic field, $B_{||}$, which is estimated by taking a 30-min, running boxcar average of the magnetic field vectors. The gray dashed curve superimposed on each of Figures 7a–7d represents the T96-model magnetic field variation along the RBSP-B trajectory.

As the growth phase proceeded, B_x (B_z) at RBSP-B increased (decreased) as a result of the tailward stretching of the near-Earth magnetic field configuration. Before ~06:00 UT, the magnetic field vectors at RBSP-B well matched with those predicted by the T96 model.

After ~06:00 UT, however, differences between the observed and modeled magnetic fields gradually became evident. In particular, the observed B_x (B_z) was larger (smaller) than the modeled B_x (B_z) by up to a few tens of nanotesla. Such a difference indicates that the near-Earth magnetic field topology at RBSP-B was more tail like than expected by T96 under these solar wind conditions.

The magnetic field components in the FA coordinate system can be used to characterize field-aligned currents (FACs) flowing at/around the plasma sheet boundary layer (PSBL) [e.g., *Ohtani et al.*, 1988]. In that case, the change in sign of B_{y_FA} together with the direction of the boundary crossing can be used to infer the polarity of the FAC flowing earthward/tailward (corresponding to the downward/upward direction in the ionosphere). For example, when a spacecraft crosses a tailward (earthward) FAC as it moves relatively in the positive Z direction, the spacecraft is expected to observe a negative (positive) excursion in B_{y_FA} . As seen in Figures 7a and 7b, the gradual increase in both $|B|$ and B_x after 0610 UT may be interpreted in terms of the thinning of the plasma sheet. The plasma sheet thinning causes magnetic flux tubes to move in the negative Z direction, i.e., in such a way as to be closer to the RBSP-B location. During this period RBSP-B slightly moved in the positive Z direction during this event (Figure 1b). Consequently, it is expected that the FAC flux tube at/around PSBL and the RBSP-B location relatively came close to each other, in particular after 0610 UT. It therefore seems to be reasonable to regard a sharp negative B_{y_FA} excursion at RBSP-B from ~06:15 to ~06:20 UT as a signature of traversing a tailward (upward) FAC. If so, the upward FAC is probably connected to the growth phase arc because the RBSP-B footprint was very close to the arc. More details of the relationship

are shown later. On the other hand, the recovery of B_{y_FA} after ~06:20 UT may be a crossing signature of earthward (downward) FAC that might form a pair with the tailward (upward) FAC.

We compare in Figure 8 the ground-based optical observations of the arc with magnetically conjugate RBSP-B measurements. The top three panels show L value (Figure 8a) at the RBSP-B location for 05:30–07:00 UT, and MLAT (Figure 8b) and MLT (Figure 8c) of its ionospheric footprint predicted by T96. For a reference, MLAT and MLT of ATHA are also shown by gray lines in Figures 8b and 8c, respectively. From Figures 8b and 8c, it is expected that an ideal RBSP-B–ATHA conjunction took place for the red-coded time interval of 0610–0620 UT in terms of MLAT and MLT. As seen in Figure 7, a reasonable agreement between the observed and modeled magnetic fields at RBSP-B assures a certain level of reliability for the conjunction. During this interval, the stretched tail field lines traced from the RBSP-B position by T96 fall into the premidnight near-tail equatorial plane at a radial distance of 5.8–6.0 R_E .

In general, understanding of the L profiles of magnetic field and plasma in the magnetosphere needs coordinated and simultaneous in situ observations at different radial distances from the Earth. However, such ideal observations seem highly unlikely. In this study, therefore, by assuming that the magnetic field and plasma at RBSP-B changed only slowly during the growth phase, we interpret the observed time sequence as the L profiles along the RBSP-B trajectory. Considering that the arc remained a quiet state at least until 06:19 UT, this assumption appears reasonable for the RBSP-B–ATHA conjunction interval. Moreover, by projecting the L profiles along the model field lines onto the ionosphere, we

can directly compare the projected profiles (i.e., latitudinal profiles) of the RBSP-B measurements with the latitudinal profiles of auroral emissions at ATHA.

Shown in Figures 8d–8g are the projected profiles of the RBSP-B measurements as a function of MLAT of the spacecraft footprint tracking for 05:30–07:00 UT. The RBSP-B measurements include the B_{y_FA} (Figure 8d), magnetic pressure (Figure 8e), HOPE/RBSPICE proton pressure (Figure 8f), and RBSPICE proton fluxes with 10–90 keV (Figure 8g). The comparisons between the observed and modeled magnetic pressure profiles, which are presented in Figure 8e, indicate that the T96 performance (dashed curve) for this event is slightly better than the TS04 one (dot-dashed curve).

For a cross check of the proton pressure between the different plasma instruments, in Figure 8f the RBSPICE proton pressure (dotted curve) derived by combining both ToF×E and ToF×PH proton products is overplotted with the HOPE pressure. There is a general good agreement between the proton pressure profiles deduced from the HOPE and RBSPICE instruments, although the values are slightly higher in RBSPICE than HOPE through most of the interval. A simple explanation of such a small difference between the RBSPICE and HOPE pressure profiles is that RBSPICE covers a larger energy range than does HOPE, and that there is substantial energy content in protons > 50 keV. The gray-shaded latitude range in Figures 8d–8g corresponds to the time (06:10–06:20 UT) when the RBSP-B–ATHA conjunction was the best in the growth phase interval (Figures 8b and 8c).

As seen in Figure 8 d, RBSP-B detected the near-tail upward FAC signature exactly during the conjunction interval. The latitudinal width of the projected upward FAC was of the order of 0.1° – 0.2° . Moreover, it is found that the upward FAC was located on the poleward

side (tailward side) of a local maximum in the proton pressure around 62° MLAT (corresponding to $L \sim 5.2\text{--}5.4$ in the inner magnetosphere) that coincided with a local minimum in the magnetic pressure (Figure 8f). As seen in Figure 8g, the proton fluxes in the energy range $\sim 20\text{--}50$ keV appear to play a primary role in formation of the spatially localized proton pressure hump.

To compare these RBSP-B measurements with the auroral emissions at ATHA, stacked latitudinal profiles of the 486.1 nm ($H\beta$) and 557.7 nm emissions measured with the co-located OMTI ASI at ATHA are presented in Figures 8h and 8i, respectively. Each of the latitudinal profiles was obtained by slicing the ASI image at each of the selected times along the south to north magnetic meridian that intersects the zenith of ATHA. Considering that the $H\beta$ (557.7 nm) auroral emissions would primarily be caused by the precipitation of protons (keV-electrons) into the ionosphere, their near-simultaneous observations allow us to distinguish between proton- and electron-dominated auroral emissions in the vicinity of the growth phase arc. The color-coded dashed vertical line at each time in Figure 8h marks the peak latitude of the $H\beta$ emissions, being a proxy of the isotropy boundary (often referred to as "b2i") for energetic ions of 3–30 keV [Donovan *et al.*, 2003]. The peak latitude of the 557.7 nm emissions (corresponding to the growth phase arc location) was located $\sim 0.1^\circ\text{--}0.4^\circ$ poleward of the b2i latitude. As time progressed both the arc and b2i gradually shifted equatorward while retaining the latitudinal separation. Such a latitudinal separation between the electron and proton auroral emission peaks is similar to that reported in earlier studies [e.g., Deehr and Lummerzheim, 2001; Dubyagin *et al.*, 2003; Lessart *et al.*, 2007].

Proton aurora in the subauroral ionosphere, which is generally considered to result from the diffuse precipitation of sub-keV to tens-of-keV protons [Donovan *et al.*, 2012], likely reflects the plasma pressure structure in the inner magnetosphere. The RBSP-B–ATHA conjunction also allows us to assess the M-I linkage between structures of the proton auroral emission (Figure 8h) along the ATHA meridian and of the proton pressure (Figure 8f) projected onto the ionosphere along the RBSP-B trajectory in the inner magnetosphere. We find a quantitative agreement between the peak locations of the projected proton pressure and the proton auroral emission, although there is a discrepancy of $\sim 0.1\text{--}0.2^\circ$ in latitude that could be due to an uncertainty of mapping predicted from the T96 model. The quantitative agreement supports that the RBSP-B location in the gray-shaded area was magnetically conjugate to the growth phase arc. Such a conjunction is also supported by the fact that for this interval RBSP-B observed a magnetic signature of the thin upward FAC sheet (Figure 8d). Given that the growth phase arc links to the upward FAC of which the projected latitudinal width is almost of the same order as the arc width ($\sim 0.1\text{--}0.3^\circ$), another implication from the in situ magnetic and plasma data is that the origin of the upward FAC is on the tailward side of a localized, small plasma pressure hump at $L \sim 5.2\text{--}5.4$.

4. Summary and Discussion

In the case study of the 1 May 2013 substorm event, we have investigated the spatiotemporal behavior and origin of the growth phase/onset arcs, using the premidnight conjugate space-ground measurements of the visible auroral evolution made by the THEMIS/OMTI ASIs, the time-dependent large-scale FAC patterns in the ionosphere by

AMPERE at ~ 780 km altitude, and the in situ information regarding the inner tail source by RBSP-B at $L \sim 5.0$ – 5.6 . Major results obtained from the conjugate M-I observations of this particular event are summarized as follows:

1. At the early stage of the growth phase, two neighboring THEMIS ASIs at ATHA and TPAS observed the quiet, east-west aligned arc (growth phase arc) that appeared around 63° MLAT and then moved gradually equatorward. At the late stage (i.e., immediately before the auroral breakup) the arc location moved down to $\sim 62^\circ$ MLAT.
2. The OMTI ASI at ATHA indicated that the location of the developing electron-dominated arc remained at a latitude ~ 0.1 – 0.4° poleward of the proton-dominated emission peak, being an indication of the isotropy boundary.
3. The THEMIS-ASI–AMPERE conjunction revealed (1) that throughout the growth phase the thin arc developed inside the R2 FAC region and (2) that the latitudinal separation between the arc and R1/R2 boundary narrowed from $\sim 4.5^\circ$ to $\sim 1.0^\circ$ as time proceeded.
4. When the ionospheric footprint of RBSP-B was ideally very close to the growth phase arc, RBSP-B observed a localized upward FAC, likely connected to the arc in the ionosphere.
5. The arc-related upward FAC was located within the tailward part of a spatially localized plasma pressure hump that developed at $L \sim 5.2$ – 5.4 in the premidnight inner magnetosphere, suggesting the role of local pressure gradients as a driver for

the upward FAC.

Where and how the growth phase/onset arcs are generated in the M-I system has been a subject of great interest in substorm dynamics. A few recent case studies [*Shiokawa et al.*, 2005; *Marghitu et al.*, 2009; *Jiang et al.*, 2012; *Nishimura et al.*, 2012] have provided a snapshot of the growth phase/onset arc location relative to large-scale FAC patterns based on the magnetic field deviations measured along a polar-orbiting spacecraft crossing the arc. In contrast to the one-time snapshot for each event, our event study has demonstrated for the first time the time-dependent (dynamical) nature of the arc location by taking advantage of AMPERE magnetic field measurements. We found that the arc near the onset region emerges around the latitudinal center of the downward R2 FAC region and then approaches near the R1/R2 boundary. Such a time-dependent picture of the arc location provides a crucial constraint on modeling the formation process of the growth phase arc in the M-I system.

Recently, *Yang et al.* [2013] carried out a numerical simulation on the formation process of a growth phase arc with a high-resolution RCM-E model, in which the spatial resolution (mean latitudinal grid spacing $\sim 0.065^\circ$ in the ionosphere) was enhanced for simulating the thin arc structure in the ionosphere in a realistic manner. The high-resolution model succeeded in reproducing the observational features of growth phase arcs shown by *Nishimura et al.* [2012], in particular the relationship of the thin arc location (local R1-sense upward FAC) with large-scale R1/R2 FAC distribution in the ionosphere. The model also demonstrated the structure and dynamics of the near-Earth tail related to the arc

formation. On the origin of the arc, the model predicted that the local upward FAC responsible for the premidnight arc maps into the tailward portion of a local high plasma pressure region at $\sim 8 R_E$ downtail, formed as a result of enhanced earthward convection (dawn-to-dusk electric field) that becomes predominant in most of the plasma sheet during the growth phase. The location is adjacent to the transition region from the dipole-like to tail-like field configuration, as well as to the region just tailward of the main R2 FAC source region. Our in situ measurements (Figure 8) from the RBSP-B spacecraft conjugate to the arc generally support such a model prediction of the arc origin. It should be noted, however, that the localized high-pressure region identified by RBSP-B in the premidnight near-Earth tail of $L \sim 5.2\text{--}5.4$ is closer to the Earth than predicted by *Yang et al.* [2013]. This discrepancy may be due to preconditioning of the background geomagnetic disturbance controlled by solar wind driver. Indeed, the IMF B_z was negative with the range of -5 and -10 nT for several hours before and during this substorm event, which would cause the arc origin to shift closer to the Earth.

Although the results shown here have highlighted reliable evidence for the M-I linkage of the growth phase arc, the formation process remains unclear. As shown in Figure 2 of *Yang et al.* [2013], the RCM-E model prediction showed that the generation of additional R1 sense FACs responsible for the growth phase arc is associated with the localized alternation in the direction of the gradient of $PV^{5/3}$ with respect to the gradient of the plasma velocity formed by an induction dawn-to-dusk electric field near the magnetic transition region. However, our in situ observations cannot test this process because there are only measurements along the single satellite pass in the magnetosphere. We also note that the

numerical simulation has not yet included effects of the small-scale processes (e.g., acceleration process) or fully investigated the time-dependent processes. To obtain better understanding of the arc formation process, further simultaneous, multipoint, ground-space measurements are required together with improved numerical simulations.

Acknowledgements.

Work at JHU/APL was supported by JHU/APL subcontract 937836 under NASA prime contract NAS5-01072 for the Van Allen Probes mission, and also partially by a NASA grant (NNX12AJ52G) and an NSF grant (GEO/ATM-110433). The research at NJIT was supported in part by Van Allen Mission subcontract 937836 under NASA Prime Contract NAS5-01072. The authors thank all of the Van Allen Probes teams for operating the spacecraft and providing each instrument's data. Most of data from the Van Allen Probe-B spacecraft used in this study are publicly available at CDAWeb (<http://cdaweb.gsfc.nasa.gov/>). RBSPICE data are also archived on the RBSPICE Science Data Center web site: <http://rbspice.ftcs.com/Data.html>. We would also like to thank the AMPERE team and the AMPERE Science Center for providing the processed AMPERE data products that are publicly available on the AMPERE website: <http://ampere.jhuapl.edu/>. In addition, the AMPERE raw $\delta\mathbf{B}$ vector data are provided by H. Korth of the JHU/APL on request. We also thank V. Angelopoulos, S. Mende, and E. Donovan for use of the THEMIS ASI data. Deployment and data retrieval of the THEMIS ASIs were supported primarily by NASA contract NAS5-02099, and partly by the Canadian Space Agency. Data from the THEMIS GBO measurements are publicly available on the THEMIS mission website:

600 <http://themis.ssl.berkeley.edu/index.shtml>. The SuperMAG ground-based magnetometer
601 and geomagnetic index data were downloaded from the SuperMAG website:
602 <http://supermag.jhuapl.edu/>. We gratefully acknowledge not only all of the organizations
603 and national agencies that operate the ground-based magnetometers, but also all of the PIs
604 for willingly providing these data to SuperMAG. The OMTIs
605 (<http://stdb2.stelab.nagoya-u.ac.jp/omti/>) have been developed and operated by Y. Katoh, M.
606 Satoh, T. Katoh, Y. Haraguchi, Y. Yamamoto, and T. Adachi of the STEL, Nagoya
607 University, and I. Schofield and K. Reiter of the Athabasca University. The OMTI data at
608 Athabasca are provided by the PI (K. Shiokawa of the STEL, Nagoya University) on
609 request. Athabasca ground facilities were installed and operated with financial support from
610 the Canada Foundation for Innovation. The SYM-H index data were obtained from WDC
611 for geomagnetism, Kyoto. The OMNI solar wind data were obtained from the GSFC/SPDF
612 OMNIWeb interface at <http://omniweb.gsfc.nasa.gov>.

References

- Akasofu, S.-I. (1964), The development of the auroral substorm, *Planet. Space Sci.*, 12, 273–282, doi:10.1016/0032-0633(64)90151-5.
- Anderson, B. J., H. Korth, C. L. Waters, D. L. Green, V. G. Merkin, R. J. Barnes, and L. P. Dyrud (2014), Development of large-scale Birkeland currents determined from the Active Magnetosphere and Planetary Electrodynamics Response Experiment, *Geophys. Res. Lett.*, 41, 3017–3025, doi:10.1002/2014GL059941.
- Baker, K. B., and S. Wing (1989), A new magnetic coordinate system for conjugate studies at high latitudes, *J. Geophys. Res.*, 94(A7), 9139–9143, doi:10.1029/JA094iA07p09139.
- Deehr, C., and D. Lummerzheim (2001), Ground-based optical observations of hydrogen emission in the auroral substorm, *J. Geophys. Res.*, 106(A1), 33–44, doi:10.1029/2000JA002010.
- Donovan, E. F., B. J. Jackel, I. Voronkov, T. Sotirelis, F. Creutzberg, and N. A. Nicholson (2003), Ground-based optical determination of the b2i boundary: A basis for an optical MT-index, *J. Geophys. Res.*, 108, 1115, doi:10.1029/2001JA009198, A3.
- Donovan, E. F., S. Mende, B. Jackel, M. Syrjäso, M. Meurant, I. Voronkov, H. U. Frey, V. Angelopoulos, and M. Connors (2006), The azimuthal evolution of the substorm expansive phase onset aurora, in *Proceedings of International Conference on Substorms-8*, edited by M. Syrjäso and E. Donovan, pp. 55–60, Univ. of Calgary, Calgary, Alberta, Canada.
- Donovan, E., Spanswick, E., Liang, J., Grant, J., Jackel, B. and Greffen, M. (2012) Magnetospheric Dynamics and the Proton Aurora, in *Auroral Phenomenology and Magnetospheric Processes: Earth And Other Planets* (eds A. Keiling, E. Donovan, F. Bagenal and T. Karlsson), American Geophysical Union, Washington, D. C.. doi:

10.1029/2012GM001241

Dubyagin, S. V., V. A. Sergeev, C. W. Carlson, S. R. Marple, T. I. Pulkkinen, and A. G. Yahnin (2003), Evidence of near-Earth breakup location, *Geophys. Res. Lett.*, 30, 1282, doi:10.1029/2002GL016569

Frey, H. U., S. B. Mende, V. Angelopoulos, and E. F. Donovan (2004), Substorm onset observations by IMAGE-FUV, *J. Geophys. Res.*, 109, A10304, doi:10.1029/2004JA010607.

Funsten, H. O., et al. (2013), Helium, Oxygen, Proton, and Electron (HOPE) mass spectrometer for the Radiation Belt Storm Probes Mission, *Space Sci. Rev.*, 179, 423–484, doi:10.1007/s11214-013-9968-7.

Gjerloev, J. W., R. A. Hoffman, M. M. Friel, L. A. Frank, and J. B. Sigwarth (2004), Substorm behavior of the auroral electrojet indices, *Ann. Geophys.*, 22, 2135–2149, doi:10.5194/angeo-22-2135-2004.

Gjerloev, J. W. (2009), A Global Ground-Based Magnetometer Initiative, *EOS*, 90, 230-231, doi:10.1029/2009EO270002.

Gjerloev, J. W. (2012), The SuperMAG data processing technique, *J. Geophys. Res.*, 117, doi:10.1029/2012JA017683.

Iijima, T., and T. A. Potemra (1978), Large-scale characteristics of field-aligned currents associated with substorms, *J. Geophys. Res.*, 83(A2), 599–615, doi:10.1029/JA083iA02p00599.

Jiang, F., R. J. Strangeway, M. G. Kivelson, J. M. Weygand, R. J. Walker, K. K. Khurana, Y. Nishimura, V. Angelopoulos, and E. Donovan (2012), In situ observations of the “preexisting auroral arc” by THEMIS all sky imagers and the FAST spacecraft, *J. Geophys. Res.*, 117, A05211, doi:10.1029/2011JA017128.

Kishabeth, J. L., and G. Rostoker (1977), Modelling of three-dimensional current systems associated with magnetospheric substorms, *Geophys. J. R. astr. Soc.*, 49, 655-683.

Kletzing, C. A., et al. (2013), The Electric and Magnetic Field Instrument Suite and Integrated Science (EMFISIS) on RBSP, *Space Sci. Rev.*, 179, 127–181, doi:10.1007/s11214-013-9993-6.

Lessard, M. R., W. Lotko, J. LaBelle, W. Peria, C. W. Carlson, F. Creutzberg, and D. D. Wallis (2007), Ground and satellite observations of the evolution of growth phase auroral arcs, *J. Geophys. Res.*, 112, A09304, doi:10.1029/2006JA011794.

Liou, K., P. T. Newell, D. G. Sibeck, C.-I. Meng, M. Brittnacher, and G. Parks (2001), Observation of IMF and seasonal effects in the location of auroral substorm onset, *J. Geophys. Res.*, 106(A4), 5799–5810, doi:10.1029/2000JA003001.

Marghitu, O., T. Karlsson, B. Klecker, G. Haerendel, and J. McFadden (2009), Auroral arc and oval electrodynamics in the Harang region, *J. Geophys. Res.*, 114, A03214, doi:10.1029/2008JA013630.

Mauk, B. H., N. J. Fox, S. G. Kanekal, R. L. Kessel, D. G. Sibeck, and A. Ukhorskiy (2013), Science objectives and rationale for the radiation belt storm probes mission, *Space Sci. Rev.*, 179, 3–27, doi:10.1007/s11214-012-9908-y.

Mende, S. B., C. W. Carlson, H. U. Frey, L. M. Peticolas, and N. Østgaard (2003), FAST and IMAGE-FUV observations of a substorm onset, *J. Geophys. Res.*, 108, 10.1029/2002JA009787.

Mende, S. B., et al. (2008), The THEMIS array of ground based observatories for the study of auroral substorms, *Space Sci. Rev.*, doi:10.1007/s11214-008-9380.

Mitchelle, D. G., et al. (2013), Radiation Belt Storm Probes Ion Composition Experiment (RBSPICE), *Space Sci. Rev.*, 179:263–308, doi:10.1007/s11214-013-9965-x.

685 Motoba, T., K. Hosokawa, A. Kadokura, and N. Sato (2012), Magnetic conjugacy of northern
686 and southern auroral beads, *Geophys. Res. Lett.*, 39, L08108,
687 doi:10.1029/2012GL051599.

688 Motoba, T., K. Takahashi, A. Ukhorskiy, M. Gkioulidou, D. G. Mitchell, L. J. Lanzerotti, G. I.
689 Korotova, E. F. Donovan, J. R. Wygant, C. A. Kletzing, W. S. Kurth, and J. B. Blake
690 (2015), Link between premidnight second harmonic poloidal waves and auroral
691 undulations: Conjugate observations with a Van Allen Probe spacecraft and a THEMIS
692 all-sky imager. *J. Geophys. Res. Space Physics*, 120, 1814–1831. doi:
693 10.1002/2014JA020863.

694 Nishimura, Y., L. Lyons, S. Zou, V. Angelopoulos, and S. Mende (2010), Substorm triggering by
695 new plasma intrusion: THEMIS all - sky imager observations, *J. Geophys. Res.*, 115,
696 A07222, doi:10.1029/2009JA015166.

697 Nishimura, Y., L. R. Lyons, T. Kikuchi, V. Angelopoulos, E. F. Donovan, S. B. Mende, and H.
698 Lühr (2012), Relation of substorm pre-onset arc to large-scale field-aligned current
699 distribution, *Geophys. Res. Lett.*, 39, L22101, doi:10.1029/2012GL053761.

700 Newell, P. T., Y. I. Feldstein, Y. I. Galperin, and C.-I. Meng (1996), Morphology of nightside
701 precipitation, *J. Geophys. Res.*, 101(A5), doi:10.1029/95JA03516.

702 Newell, P. T., and J. W. Gjerloev (2011a), Evaluation of SuperMAG auroral electrojet indices as
703 indicators of substorms and auroral power, *J. Geophys. Res.*, 116, A12211,
704 doi:10.1029/2011JA016779.

705 Newell, P. T., and J. W. Gjerloev (2011b), Substorm and magnetosphere characteristic scales
706 inferred from the SuperMAG auroral electrojet indices, *J. Geophys. Res.*, 116, A12232,
707 doi:10.1029/2011JA016936.

708 Ohtani, S., S. Kokubun, R. C. Elphic, and C. T. Russell (1988), Field-aligned current signatures

in the near-tail region: 1. ISEE observations in the plasma sheet boundary layer, *J. Geophys. Res.*, 93(A9), 9709–9720, doi:10.1029/JA093iA09p09709.

Ohtani, S., S. Wing, P. T. Newell, and T. Higuchi (2010), Locations of night-side precipitation boundaries relative to R2 and R1 currents, *J. Geophys. Res.*, 115, A10233, doi:10.1029/2010JA015444.

Russell, C. T., et al. (2008), THEMIS ground-based magnetometers, *Space Sci. Rev.*, doi:10.1007/s11214-008-9337-0.

Sergeev, V., Y. Nishimura, M. Kubyshkina, V. Angelopoulos, R. Nakamura, and H. Singer (2012), Magnetospheric location of the equatorward prebreakup arc, *J. Geophys. Res.*, 117, A01212, doi:10.1029/2011JA017154.

Shiokawa, K., K. Yago, K. Yumoto, D. G. Baishev, S. I. Solov'yev, F. J. Rich, and S. B. Mende (2005), Ground and satellite observations of substorm onset arcs, *J. Geophys. Res.*, 110, A12225, doi:10.1029/2005JA011281.

Shiokawa, K., Y. Otsuka, and T. Ogawa (2009), Propagation characteristics of nighttime mesospheric and thermospheric waves observed by optical mesosphere thermosphere imagers at middle and low latitudes, *Earth Planets Space*, 61, 479–491.

Tsyganenko, N. A., and D. P. Stern (1996), Modeling the global magnetic field of the large-scale Birkeland current systems, *J. Geophys. Res.*, 101, 27,187–27,198.

Tsyganenko, N. A. and Sitnov, M. I. (2005), Modeling the dynamics of the inner magnetosphere during strong geomagnetic storms, *J. Geophys. Res.*, 110, A03208, doi:10.1029/2004JA010798.

Weimer, D. R. (1994), Substorm time constants, *J. Geophys. Res.*, 99, 11,005–11,015, doi:10.1029/93JA02721.

Yago, K., K. Shiokawa, K. Hayashi, and K. Yumoto (2005), Auroral particles associated with a

733 substorm brightening arc, *Geophys. Res. Lett.*, 32, L06104,
734 doi:10.1029/2004GL021894.

735 Yago, K., K. Shiokawa, K. Yumoto, D. G. Baishev, S. I. Solovyev, and F. J. Rich (2007),
736 Simultaneous DMSP, all-sky camera, and IMAGE FUV observations of the brightening
737 arc at a substorm pseudo-breakup, *Earth Planets Space*, 59, 45–49

738 Yang, J., R. A. Wolf, F. R. Toffoletto, and S. Sazykin (2013), RCM-E simulation of substorm
739 growth phase arc associated with large-scale adiabatic convection, *Geophys. Res. Lett.*,
740 40, 6017–6022, doi:10.1002/2013GL058253.

Figure Captions

Figure 1. Location of the Van Allen Probe B (RBSP-B) spacecraft for the interval from 05:30 UT to 07:00 UT on 1 May 2013, projected into the SM (a) x - y and (b) x - z planes. The dashed line in the x - y plane indicates geosynchronous orbit. Magnetic field lines derived from the T96 model (gray curves) and magnetic latitudes of $\pm 15^\circ$ from the equator (dashed lines) are also shown in the x - z plane as a reference. (c) The geographic locations of the THEMIS GBO stations, Fort Smith (labeled FSMI), Athabasca (labeled ATHA), and The Pas (labeled TPAS) employed in this study, together with the field-of-views of the all-sky imagers. The AACGM latitudes are drawn every 2 degrees. The magnetic footprint at 110 km altitude of the RBSP-B spacecraft is shown with solid orange circle marks indicating the satellite position at 30-min intervals. The green lines with solid circle marks at 19.44-s intervals indicate the pre-midnight AMPERE tracks at early (i), middle (ii), and late (iii) stages of the substorm growth phase discussed in the text.

Figure 2. Interplanetary magnetic field (IMF) and geomagnetic activity conditions from 00:00 UT to 12:00 UT on 1 May 2013: (a) IMF $|B|$, (b) IMF B_y (blue) and B_z (red), (c) SMU/SML/SMLd (see the text) indices, and (d) SYM H index. Gray shaded area between 05:30 UT and 07:00 UT includes the substorm interval presented here.

Figure 3. Temporal variations of the 1 May 2013 substorm derived from both ASIs and magnetometers at three THEMIS GBO stations, FSMI, ATHA, and TPAS. (Left) Selected snapshots of (a-d) THEMIS ASIs data, projected onto the geographic coordinates. (Right) Keograms from (e) FSMI, (f) ATHA, and (g) TPAS. (h) N -component and (i) Z -component of the magnetograms at FSMI (yellow), ATHA (red), and TPAS (blue). Vertical dashed line indicates the onset of auroral breakup at $\sim 06:24:36$ UT.

Figure 4. Snapshots depicting the growth phase/onset arcs and subsequent expansion observed with two neighboring ASIs at ATHA (left) and TPAS (right) for the time interval of 06:15–06:25 UT. Shown is time sequence of partial images (256×64 pixel, corresponding to one fourth of the field of view) at 1-min intervals. The ATHA (TPAS) partial images were collected roughly from the center (bottom) of each ASI field-of-view. Overplotted are MLAT contours of 62.0° , 62.5° ,

and 63.0° and MLT meridian of 22:00 MLT (23:00 MLT) in the ATHA (TPAS) images. The RBSP-B footprint (red circle) is also superimposed onto each of the ATHA images.

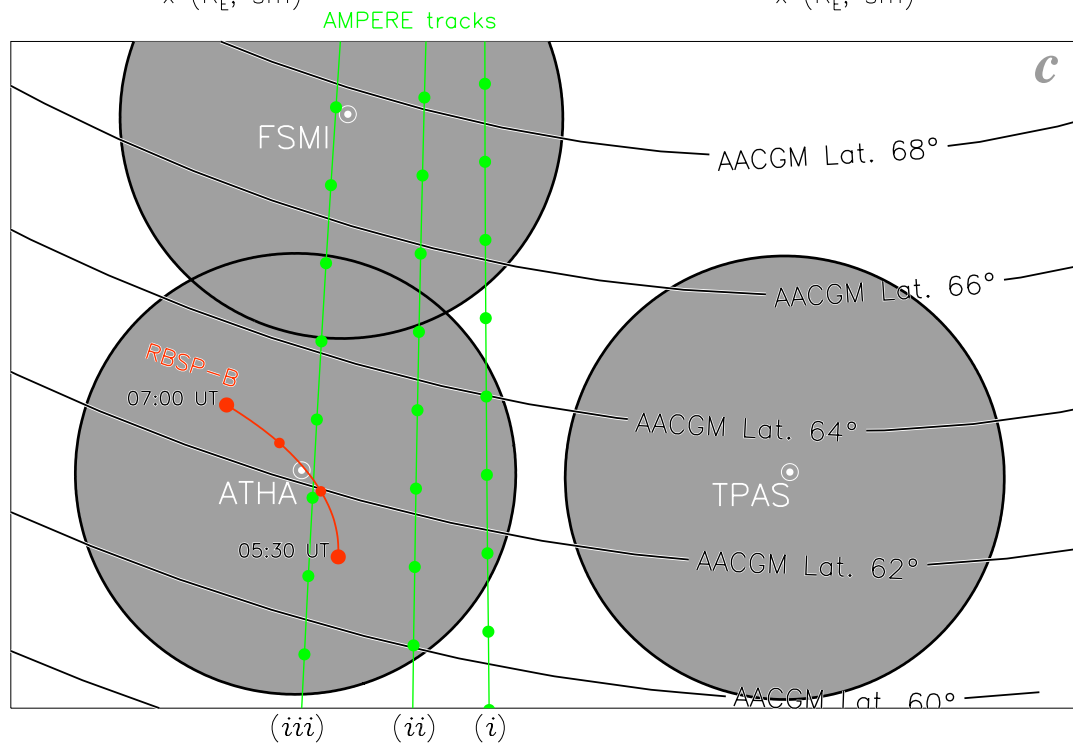
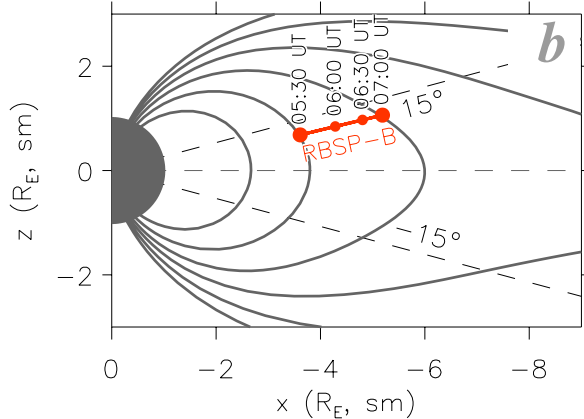
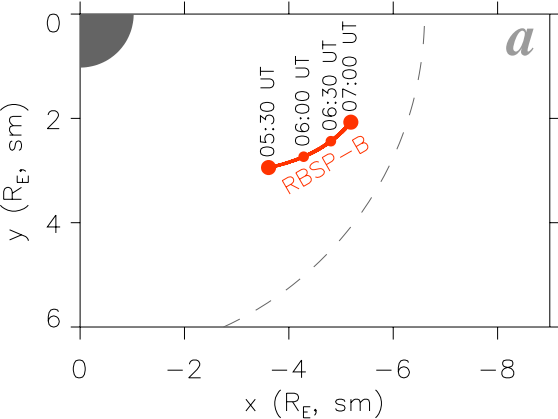
Figure 5. Examples of 2D comparison of the THEMIS ASI auroral emissions and AMPERE-derived FACs in the pre-midnight sector at 06:16 UT and 06:24 UT. The red and blue contours indicate the upward and downward FACs deduced by fitting the AMPERE data for 06:12–06:22 UT (06:20–06:30 UT) to a spherical harmonic function in the top (bottom) panel. The yellow vectors denote the raw $\delta\mathbf{B}$ perturbations along the particular pre-midnight AMPERE orbital track that moved in the poleward direction during the interval of 06:14–16:18 UT (06:22–06:26 UT) in the top (bottom) panel.

Figure 6. Comparisons between the latitudinal profiles of (a) the AMPERE raw $\delta\mathbf{B}$ perturbations (red: east, blue: north), (b) auroral luminosity along the pre-midnight AMPERE orbital track, (c) auroral images at ATHA and FSMI, and (d) SuperMAG magnetic field disturbances (red: N -component, blue: Z -component) at selected ten stations, at the (i) early, (ii) middle, and (iii) late stages of the growth phase. The all-sky images in panel (c) are taken at the closest time when an Iridium vehicle passed over the arc. Red (black) dashed line indicates the latitude of the arc (R1/R2 boundary) derived from the auroral intensity (AMPERE raw $\delta\mathbf{B}$) profile. The red (blue) dashed curve in panel (d) indicates a spline fit to a set of the N -component (Z -component) deviation data.

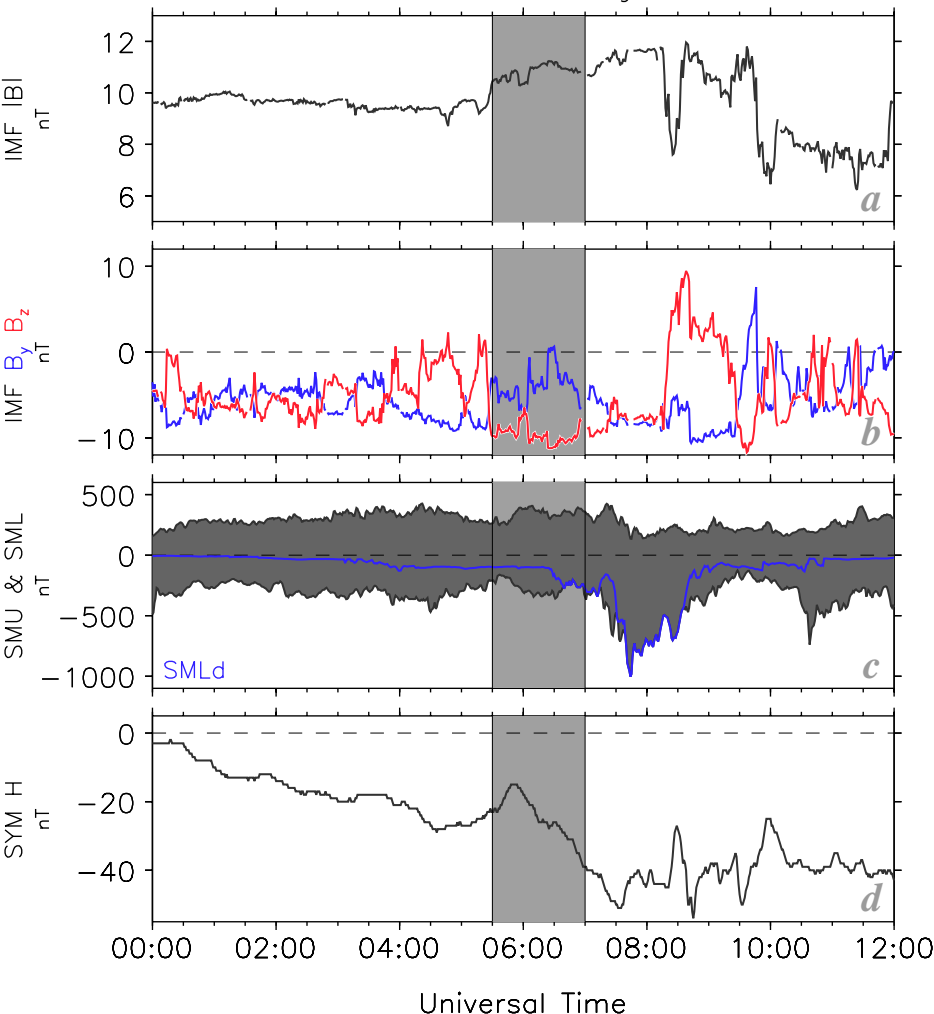
Figure 7. Magnetic field variations measured at the Van Allen Probe-B spacecraft from 05:30 UT to 07:00 UT on 1 May 2013. (a) The magnetic field strength ($|B|$), (b) B_x , (c) B_y and (d) B_z components in GSM coordinates, and (e) B_{x_FA} and (f) B_{y_FA} components in field-aligned (FA) coordinates. The B_{x_FA} (B_{y_FA}) component in FA coordinates is directed radially outward (eastward).

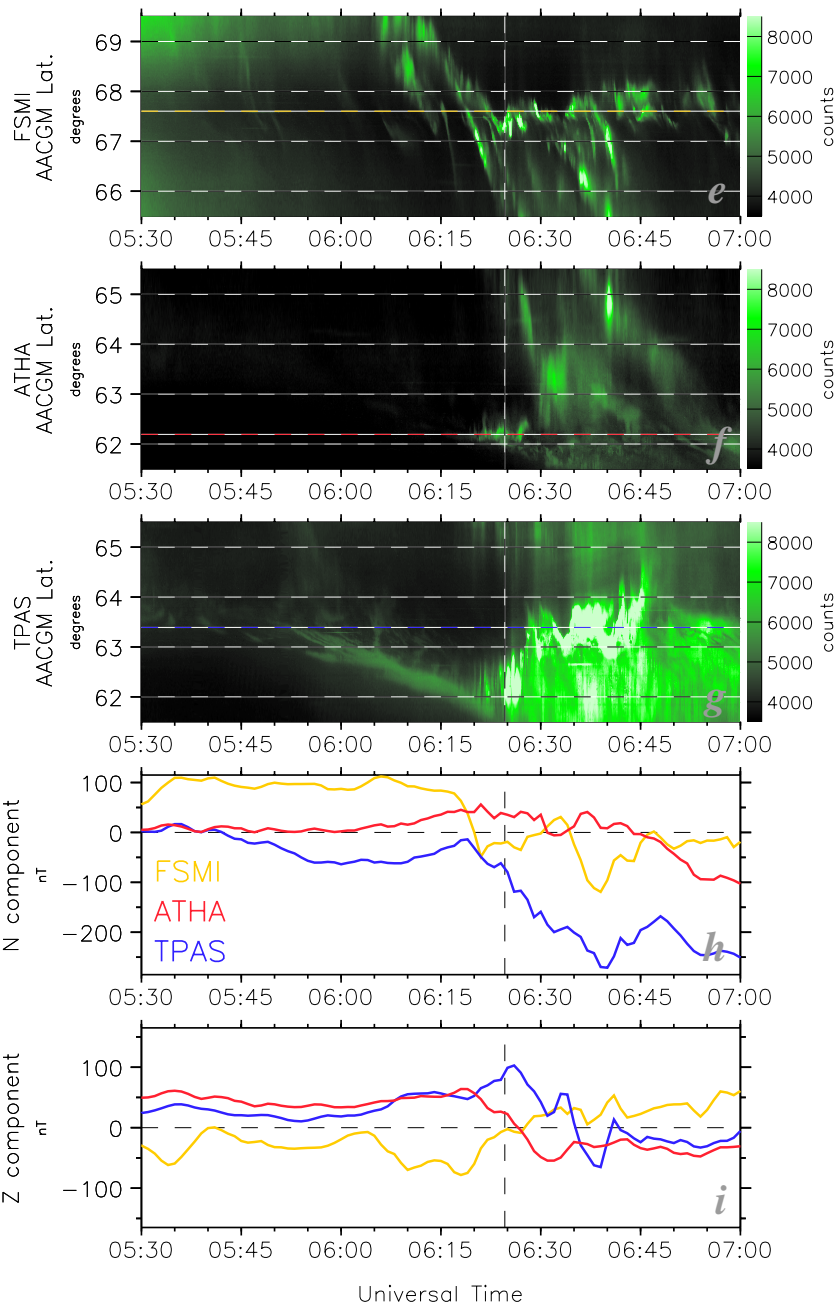
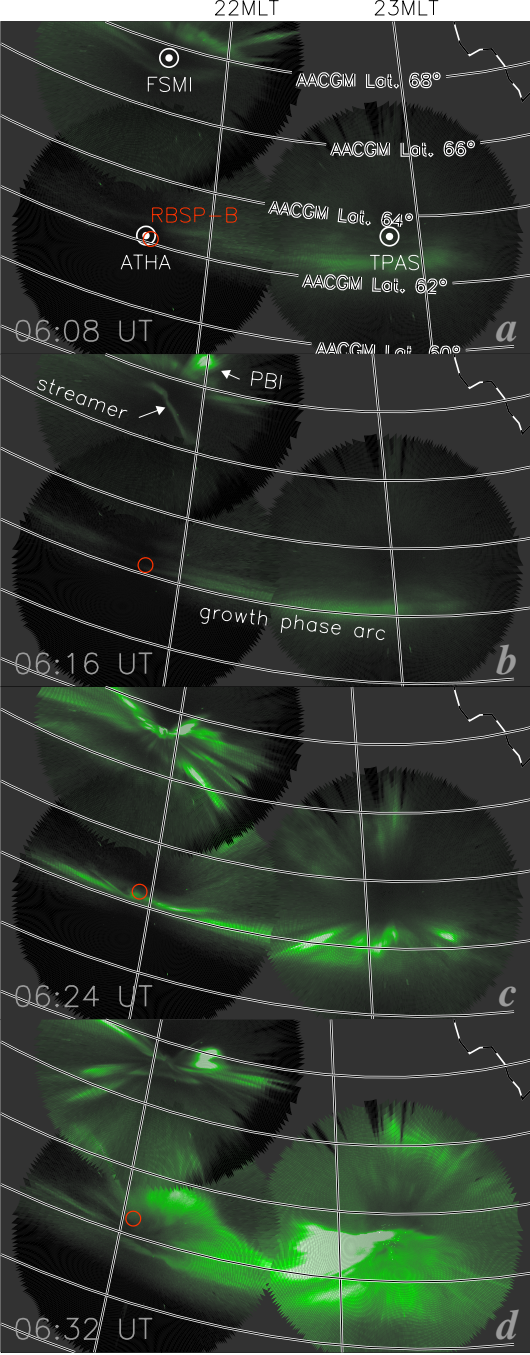
Figure 8. An overview of conjugate space-ground observations on 1 May 2013. (a) L value at the Van Allen Probe B spacecraft location from 05:30 to 07:00 UT. (b) MLAT and (c) MLT of the spacecraft footprint, together with MLAT and MLT of ATHA (gray curve). The curves are red-coded for the period when the spacecraft footprint was the best conjunction with ATHA in terms of MLAT and MLT. (d) B_{y_FA} component in FA coordinates, (e) magnetic pressure (solid curve: observation, dashed curve: T96 model, dot-dashed curve: TS04 model), (f) plasma

pressure (black thick line: HOPE, gray dotted line: RBSPICE), and RBSPICE energetic proton
fluxes with 10–90 keV obtained from in situ measurements at the Van Allen Probe-B spacecraft.
All of the spacecraft parameter data are represented as a function of MLAT of the spacecraft
footprint. Each of the curves is also red-coded for the same period as Figures 8a–8c. Stacked
latitudinal profiles of (g) 486.1-nm ($H\beta$) and (h) 557.7-nm auroral emissions every 2 min
obtained from the OMTI ASI measurements at ATHA for the interval of 06:10–06:18 UT. The
red triangle is the zenith of ATHA.

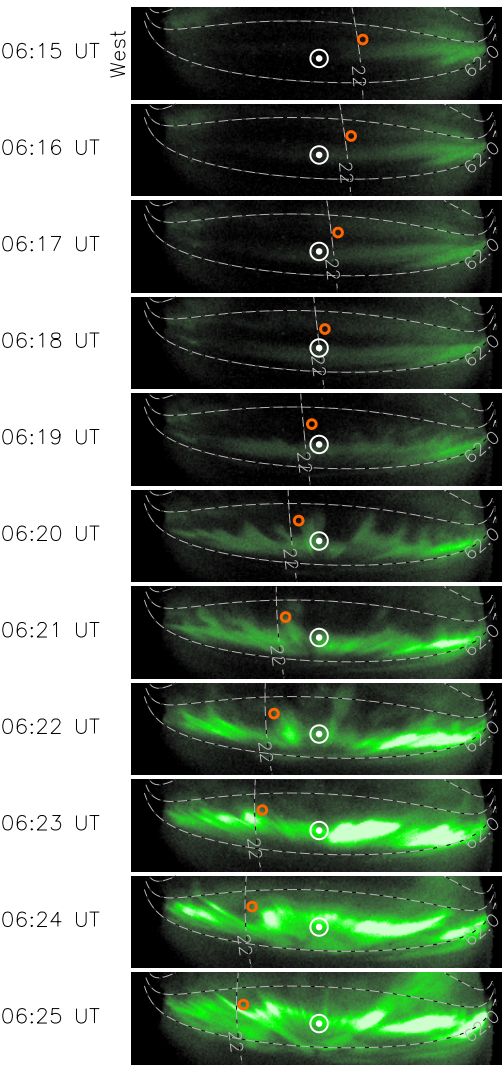


OMNI Solar Wind and Geomagnetic Indices





2013-05-01 ATHA



2013-05-01 TPAS

